Applied Surface Science 648 (2024) 159029

Contents lists available at ScienceDirect

Applied Surface Science

journal homepage: www.elsevier.com/locate/apsusc

Full length article

A DFT study of elementary reaction steps of dry reforming of methane catalyzed by Ni: Explaining the difference between Ni particles supported on CeO_2 and MnO_x-doped CeO_2

Lea Gašparič [a,b], Albin Pintar [c], Anton Kokalj [a,b,*]

[a] Department of Physical and Organic Chemistry, Jožef Stefan Institute, Jamova 39, SI-1000 Ljubljana, Slovenia
[b] Jožef Stefan International Postgraduate School, Jamova 39, SI-1000 Ljubljana, Slovenia
[c] Department of Inorganic Chemistry and Technology, National Institute of Chemistry, Hajdrihova 19, SI-1001 Ljubljana, Slovenia

ARTICLE INFO

Keywords:
Methane dry reforming
Nickel
DFT calculations
Reaction mechanism

ABSTRACT

With the aid of DFT calculations, we investigate the elementary reaction steps of dry reforming of methane (DRM) on Ni(111) and NiO(100) as simple models of metallic and oxidized Ni catalysts. The reaction-path calculations reveal that DRM is feasible on metallic Ni at elevated temperatures. However, a notable problem with metallic Ni catalysts is the coke formation because the activation barrier for the C* formation is not considerably higher than those of the competing reactions that lead to the DRM products. In contrast, NiO does not encounter issues with coke formation, but it is not an effective catalyst due to too high activation energies and slow surface diffusion of H*. We also explain the experimentally observed difference between the DRM catalysts consisting of Ni particles supported on undoped and MnO_x-doped CeO_2 supports (designated as Ni/CeO_2 and Ni/Mn_xCeO_2, respectively). Specifically, we explain the absence of the 2020 cm^{-1} vibrational peak on the Ni/Mn_xCeO_2 catalyst. Calculations univocally attribute the experimentally observed 2020 cm^{-1} peak to CO adsorbed on a top site of metallic Ni because all other sites and involved species display considerably different frequencies. The CO stretching frequency increases as Ni oxidizes, and on NiO(100), it is similar to the vibration of CO on the CeO_2(111) support, about 2100 cm^{-1}. Current results thus provide a sound explanation of why Ni/Mn_xCeO_2 is a superior DRM catalyst to Ni/CeO_2. In particular, the presence of the 2020 cm^{-1} peak on the Ni/CeO_2 catalyst signals that Ni particles are sufficiently metallic and thus susceptible to carbon poisoning. In contrast, the absence of the 2020 cm^{-1} peak on the Ni/Mn_xCeO_2 catalyst indicates that Ni particles are oxidized, i.e., the Ni oxidation is low enough to allow the DRM reaction but high enough to reduce the catalyst's carbon poisoning.

1. Introduction

Greenhouse gas emissions and global warming are becoming increasingly important, and considerable scientific efforts are devoted to developing more nature-friendly processes for energy conversion. Dry reforming of methane (DRM) is of great interest because it converts two major greenhouse gasses (CH_4 and CO_2) into syngas (a mixture of H_2 and CO) which can be further used in the chemical industry or as a synfuel [1]. DRM is a strongly endothermic process [2], i.e.:

$$CH_4 + CO_2 \longrightarrow 2CO + 2H_2, \quad \Delta_r H^\circ_{298\ K} = 247\ \text{kJ/mol} = 2.56\ \text{eV}. \tag{1}$$

A notable problem in catalyzed DRM is coke formation [3,4] especially at lower temperatures [5,6]. Therefore, a search for highly efficient catalysts is very active, particularly in the experimental community [4,7–9]. Noble metals are known to be effective catalysts with low coke formation, but they are expensive and scarce. Ni-based catalysts are a good alternative [4,8], but they are known to have problems with coke deposition [3]. The two most used approaches to increase the activity of Ni and reduce coke formation are alloying Ni particles with other metals [4,10–14] and tuning the metal–support interaction [4,8,9,15–18]. Among supports, CeO_2 (ceria) is considered one of the more promising due to its oxygen storage capacity, acid–base centers, and redox properties [9].

In addition to experimental approaches, various computational approaches are employed to study the DRM mechanism and the impact of experimental conditions on the reaction. Gibbs energy minimization

* Corresponding author at: Department of Physical and Organic Chemistry, Jožef Stefan Institute, Jamova 39, SI-1000 Ljubljana, Slovenia.
E-mail address: tone.kokalj@ijs.si (A. Kokalj).
URL: http://www.ijs.si/ijsw/K3-en/Kokalj (A. Kokalj).

https://doi.org/10.1016/j.apsusc.2023.159029
Received 23 September 2023; Received in revised form 17 November 2023; Accepted 26 November 2023
Available online 2 December 2023

is used to illuminate the effect of pressure, temperature, and the ratio of reactants on the reaction rate [6,19–23]. Density-functional theory (DFT) calculations with and without microkinetic modeling are used to study elementary reaction steps of methane and CO_2 decomposition on different metal surfaces [24–31]. On Ni(111), either the first H abstraction of CH_4 or the oxidation of either CH or C is reported as a rate-limiting step and CO_2 decomposes directly to CO + O [25–27,31]. Some authors [27,28] also raised a problem of strong adsorption of CO, which accumulates on the surface and promotes coke deposition.

Catalysts consisting of supported metal nanoparticles were also investigated. The CH_4 molecule is reported to adsorb on metallic particles dissociatively [4,32,33], while CO_2 can also adsorb on the support, especially in the vicinity of metal particles [4,17,33–35]. For Ni nanoparticles on ceria support, there is a significant charge transfer between the Ni nanoparticle and the support, where Ni atoms at the interface are oxidized to +1 or +2 oxidation states, and cerium ions are reduced [36,37]. This effect results in the strong metal–support interaction, which is reported to be important for activating the CH_4 molecule [38,39]. Although Ni nanoparticles are considered to be in a metallic state during the reaction, there are reports about the importance of nickel carbide and nickel oxide for the DRM process [40,41] where NiO tends to be coke resistant [42]. Before catalytic tests, Ni catalysts are activated in a reducing atmosphere, converting NiO to metallic Ni [43–45]. The degree of reduction depends on the catalyst composition, as shown for NiO–Mg–ZrO_2 solid solution [43,46,47], and active catalysts can therefore contain different percent of NiO.

Sagar et al. [1] investigated undoped and MnO_x-doped Ni/CeO_2 as possible catalysts for DRM. They reported that MnO_x doping increases the specific surface area of the catalyst, and the number of oxygen vacancies and mobile oxygen species in the support. The MnO_x-doped catalyst (labeled herein as Ni/Mn_xCeO_2) also showed enhanced coking resistance and higher conversion rates of methane and CO_2. DRIFTS spectra of the DRM process revealed the presence of a 2020 cm^{-1} peak on the Ni/CeO_2 catalyst but not on Ni/Mn_xCeO_2. To explain this observation, the authors suggested a change in reaction mechanism from a direct dissociation of methane to a reaction between methane and the surface oxygen species.

The present study aims to scrutinize the reaction mechanism of DRM on the Ni/CeO_2 and Ni/Mn_xCeO_2 catalysts and to explain the origin of the presence and the absence of the 2020 cm^{-1} peak on the two catalysts. To this end, we performed DFT vibrational calculations to identify the species responsible for the aforementioned peak. To get further insight into the reaction mechanism of DRM, the activation and reaction energies were calculated with DFT for elementary reaction steps on Ni(111) and NiO(100). The two surfaces were used as simplified models of reduced and oxidized Ni nanoparticles to address the possibility of different oxidation states of Ni supported on CeO_2 and Mn_xCeO_2. While the DRM reaction mechanism on Ni(111) has already been extensively studied with DFT [25–29], to our knowledge, on NiO(100) it was not.

2. Technical details

2.1. DFT calculations

DFT calculations were performed with Quantum ESPRESSO [48,49] using the generalized-gradient approximation (GGA) of Perdew–Burke–Ernzerhof (PBE) [50]. NiO was described with the PBE+U scheme [51,52], using the self-consistently determined U parameter of 4.6 eV for the Ni ions as calculated with the hp.x code [53]. Kohn–Sham orbitals were described using a plane-wave basis, whereas core electrons were described implicitly with ultrasoft pseudopotentials [54,55]. For Ni and NiO systems, a wave-function cutoff of 30 Ry and a charge density cutoff of 300 Ry were used. In contrast, the respective cutoffs for alloy structures involving Mn were 50 and 500 Ry due to a harder Mn pseudopotential.

As two simplified models for supported Ni particles in different oxidation states, ferromagnetic Ni and antiferromagnetic NiO were used to represent fully metallic and fully oxidized Ni particles, respectively (these two models can thus be seen as the two limiting cases). In addition, Ni(100) with chemisorbed O atoms up to 1 monolayer (ML) coverage was used as a simplified model of partially oxidized Ni particles. As a simple model of the NiMn surface alloy, a Ni(100)–(2×2) supercell with one surface Ni atom replaced with Mn was used. This model is designated as $NiMn_x$(100). The Ni(111), Ni(100), $NiMn_x$(100), and NiO(100) slabs consisted of four (100) layers and Ni(110) of six (110) layers. The thickness of a vacuum separating the slab periodic replicas along the surface normal direction was set to a 12 Å. Adsorbates were adsorbed on the top side of the slab and the atoms in the slab's bottom layer were constrained to bulk positions, except for Ni(110), for which the two bottommost layers were fixed. All other degrees of freedom were relaxed. The in-plane lattice spacing was set to the calculated equilibrium bulk lattice parameter of 3.52 Å for Ni and 4.23 Å for NiO.[1] Brillouin-zone integrations were performed with the special point technique [56] using a Methfessel-Paxton smearing [57] of 30 mRy for Ni and 1 mRy for NiO.

CeO_2(111) was described with a slab consisting of three O–Ce–O trilayers with the bottom trilayer constrained to bulk positions. The in-plane lattice spacing was set to the calculated equilibrium bulk lattice parameter of 5.51 Å. The wave-function kinetic energy cutoff was set to 50 Ry, and the cutoff for the charge density was 500 Ry. Marzari–Vanderbilt smearing [58] of 20 mRy and the self-consistently determined U parameter of Ce ions of 4.7 eV were used.

Vibrational frequencies were calculated with the PHonon code from the Quantum ESPRESSO suite, using the density-functional perturbation theory [59]. Only the adsorbed molecule and the two upper layers of Ni(111), Ni(110), Ni(100), $NiMn_x$(100), and CeO_2(111) were perturbed. In contrast, for NiO(100), only the topmost layer was perturbed. Vibrational properties of isolated molecules were calculated with a 15 Å large cubic box using the gamma k-point. For vibrational calculations, Ni(111)–(2 × 2), Ni(100)–(2 × 2), $NiMn_x$(100)–(2×2), Ni(110)–(2 × 2), NiO(100)–(1 × 2), and CeO_2(111)–(1x1) supercells were used with the 6 × 6 × 1, 6 × 6 × 1, 6 × 6 × 1, 6 × 4 × 1, 6 × 3 × 1, and 3 × 3 × 1 uniformly shifted k-point grids, respectively.

Elementary reaction steps involved in the DRM reaction were modeled on Ni(111) and NiO(100) as the minimum-energy paths using the climbing-image nudged-elastic band (CI-NEB) method [60,61]. For NEB calculations, larger supercells were utilized than for the vibrational calculations, i.e., Ni(111)–(3 × 3) and NiO(100)–(2 × 2), for which the 4 × 4 × 1 and 3 × 3 × 1 uniformly shifted k-point grids were used, respectively.

The supercells utilized for vibrational and NEB calculations are shown in Fig. S1 in the Supplementary material.

2.2. Energy equations

Adsorption energies were calculated as:

$$E_{ads} = E_{A/slab} - E_A - E_{slab}, \quad (2)$$

where $E_{A/slab}$ is the energy of the adsorbate/slab system, and E_A and E_{slab} are the energies of isolated adsorbate species and bare slab, respectively.

Reaction energies were calculated as:

$$\Delta E = E_{FS} - E_{IS}, \quad (3)$$

[1] The two reported lattice parameters refer to a cubic unit cell. However, the calculations of antiferromagnetic NiO were performed with a supercell to accommodate spin-up and spin-down polarized Ni ions.

Table 1
The calculated frequencies of the C–O stretching vibration (in cm^{-1}) for CH_xO species ($x = 0, 1, 2$) either isolated or adsorbed on Ni surfaces. The available experimental values are written in parentheses. $CO_{(top)}$ and $CO_{(hollow)}$ stand for CO adsorbed on a top and hollow (hcp for Ni(111)) site, respectively.

	CO or $CO_{(top)}$	$CO_{(hollow)}$	CHO	CH_2O
Isolated	2107 (2169)[a]		1838	1740 (1746)[a]
Ni(111)	2005 (2045)[b]	1773 (1817)[b]	1292	1091
Ni(100)	1997 (2024)[c]	1641 (1710)[c]		
Ni(110)	1986 (1984)[d]			

[a] Ref. [2].
[b] Ref. [62].
[c] Ref. [63].
[d] Ref. [64].

Table 2
The calculated frequencies of the C–O stretching vibration (in cm^{-1}) for the CO molecule adsorbed on various surfaces.

	$CO_{(top)}$	$CO_{(hollow)}$
Ni(111)	2005	1773
Ni(110)	1986	
Ni(100)	1997	1641
$NiMn_x$(100)	1984 @ Ni	
$NiMn_x$(100)	1958 @ Mn	
Ni(100) + O(1/4 ML)		1657
Ni(100) + O(1/2 ML)	2049	
$NiMn_x$(100) + O(1/2 ML)	2071 @ Mn	
Ni(100) + O(3/4 ML)	2057	
NiO(100)	2086	
CeO_2(111)	2100	

where E_{FS} and E_{IS} are the energies of the final and initial state of an elementary reaction step, respectively. Activation energies were calculated as:

$$E^{act} = E_{TS} - E_{IS}, \quad (4)$$

where E_{TS} is the energy of the transition state obtained with the CI-NEB calculation. If a reaction step consists of more than one transition state, the TS with the highest energy is used for E_{TS}. For some cases on NiO(100), the relaxation of two reaction intermediates (say, A and B) resulted in an associated AB species. In such cases, the activation energy of the A + B ⟶ AB reaction was set to 0, while the reaction energy was calculated by the constrained relaxation, where the "docking" atoms[2] of the A and B fragments were fixed in the lateral direction.

2.3. Other definitions

Adsorbed species are indicated with an asterisk. With this notation, the adsorption of species A is written as A + * ⟶ A*, where * represents an adsorption site. The formate HCOO intermediate can adsorb as monodentate and bidentate. The two adsorption modes are labeled as HCOO* and HCOO** to indicate that monodentate binds to the surface with one and bidentate with two O atoms.

Surface coverage in monolayer (ML) units is defined as the inverse of the number of surface Ni atoms per adsorbate; for example, if Ni(100)–($N \times N$) supercell contains one adsorbate then the corresponding coverage is $1/N^2$ ML.

3. Results and discussion

First, the analysis of vibrational frequencies is presented to identify which species corresponds to the experimentally-observed 2020 cm^{-1} peak. This peak was observed on the Ni/CeO_2 catalyst but not on the Ni/Mn_xCeO_2 one [1]. Then, the effect of doping Ni with Mn is addressed. Finally, the reaction mechanism for the dry reforming of methane on Ni(111) and NiO(100) is analyzed.

3.1. Vibrational analysis

Sagar et al. [1] ascribed the 2020 cm^{-1} peak to the CH_xO species. Hence, the vibrational analysis was performed for CO, CHO, and CH_2O species adsorbed on Ni(111); isolated species and CO adsorbed on other Ni surfaces were also considered for comparison. The calculated and experimental C–O stretching frequencies are reported in Table 1, whereas other molecular frequencies of CHO and CH_2O are reported in Table S1 in the Supplementary material. The DFT calculated frequencies are lower than the experimental ones and the highest difference between them is about 70 cm^{-1}. Even when this discrepancy is taken into account, the only calculated frequency close enough to 2020 cm^{-1} is that of CO adsorbed on a top site of Ni surfaces; note that all three surface terminations give similar value of about 2000 cm^{-1}. This value agrees well with the experimentally determined value of 2017 cm^{-1} for CO on Ni/CeO_2 [65]. The calculated frequency of isolated CO is too high (2107 cm^{-1}) and that of adsorbed CHO (1292 cm^{-1}) and CH_2O (1091 cm^{-1}) on Ni(111) are much too low.

Campuzano et al. [62] showed that CO adsorbs to a three-fold hollow site on Ni(111) at lower coverages, then at a bridge site, and, at higher coverages, also at a top site. DFT calculations agree with this trend, i.e., CO adsorbs the strongest to an hcp site (−1.83 eV), followed by an fcc (−1.80 eV) and bridge (−1.71 eV) sites, and finally a top site (−1.49 eV). The calculated stability difference between the hcp and top sites is considerable. In reality, this difference is likely smaller because it is well-known that DFT favors CO adsorbed to hollow rather than top sites [66–68]. Moreover, actual catalysts consist of Ni nanoparticles that possess a significant fraction of kink and step sites, which are more likely to bind CO on top sites.

Our results suggest that the 2020 cm^{-1} peak is due to CO adsorbed on a top site of metallic Ni particles; note that CO adsorbed on top sites of different low Miller index Ni surfaces displays similar frequencies (Table 2). CO is the product of the DRM reaction hence it has to be present on both Ni/CeO_2 and Ni/Mn_xCeO_2 catalysts. Because both catalysts contain Ni particles, the absence of 2020 cm^{-1} peak on one of them suggests a change in the chemical nature of Ni particles which influences their interaction with CO. Sagar et al. [1] reported that Ni/Mn_xCeO_2 has a higher content of mobile oxygen in the support structure than the Ni/CeO_2 catalyst. This could result in more oxidized Ni particles on the Mn_xCeO_2 support. Mn ions present in the support could also alloy with Ni nanoparticles, changing their chemical characteristics. For this reason, the frequencies of the stretching vibration of CO adsorbed on O/Ni(100), O/$NiMn_x$(100), and NiO(100) were also calculated and are presented in Table 2, where O/Ni(100) and NiO(100) are used as simple models of partially and fully oxidized Ni, respectively, and O/$NiMn_x$(100) is used as a simple model of partially oxidized Ni doped with Mn. The calculated CO stretching frequency on CeO_2(111) is also given for comparison.

On Ni(100) with 0.25 ML of O*, CO preferentially adsorbs on a four-fold hollow site and the frequency is expectedly low (Table 2). At higher O* coverage, CO adsorbs on a top site with more than 50 cm^{-1} higher frequencies than on the top position of bare Ni(100). On NiO(100), the CO stretching frequency is about 90 cm^{-1} higher than on metallic Ni, which can be attributed to a weaker CO adsorption on the oxide surface; the calculated adsorption energies of CO are tabulated in Table S2 and the corresponding analysis is presented in Fig. S2 in the Supplementary material. As mentioned above, the DFT calculated frequencies are lower than the experimental ones. Therefore, we can argue that already at 0.5 ML of O*, the calculated CO frequency (2049 cm^{-1}) cannot match the experimentally observed 2020 cm^{-1} value. Hence, a partial oxidation of Ni particles on Mn_xCeO_2 support would explain the absence of 2020 cm^{-1} peak. Interestingly, the calculated frequency of CO adsorbed on CeO_2(111) is 2100 cm^{-1}, thus being similar to the

[2] A docking atom is an atom with which a fragment bonds to the surface.

value on NiO(100). Therefore, we can assume that the 2100 cm^{-1} peak, observed by Sagar et al. [1], corresponds to CO adsorbed on oxide surfaces, which do not weaken the C–O bond as much as metallic Ni (Table S2).

3.2. Ni doped with Mn

Here, we address the possibility that Mn from the Mn_xCeO_2 support could alloy with Ni particles. According to our calculations, a $NiMn_x$ alloy is thermodynamically stable. The mixing energy[3] for the bulk $NiMn_x$ alloy, where 25% of Ni atoms is replaced with Mn atoms, is −0.77 eV/Mn-atom. Moreover, a mixing entropy would further favor alloy formation, particularly at higher temperatures. Mn atoms show a slight tendency toward surface segregation, i.e., the $NiMn_x$(100)–(2×2) structure with Mn atom in the surface layer is by 0.04 eV more stable than the analogous structure with Mn atom in the bulk layer, as estimated by the seven-layer thick slab. Although the thermodynamic stability of the $NiMn_x$ alloy does not yet prove that Ni particles supported on Mn_xCeO_2 are doped with Mn, it renders the possibility sufficiently realistic to consider its implications.

On the $NiMn_x$(100) surface alloy, CO binds to the Ni atom by about 0.5 eV stronger than to the Mn atom (Table S2). The corresponding CO stretching frequencies are 1984 and 1958 cm^{-1} on top of Ni and Mn atoms (Table 2), respectively. Since Sagar et al. did not report any frequency in the 1960–2100 cm^{-1} range for the Ni/Mn_xCeO_2 catalyst, we can argue that the $NiMn_x$ alloy by itself cannot explain the difference in the observed IR vibrations. In contrast, on a partially oxidized $NiMn_x$(100) surface, modeled with $NiMn_x$(100) covered by 1/2 ML of O*, the CO stretching frequency is 2071 cm^{-1} (Table 2), which, taking into account that calculations underestimate the frequencies, would correspond to the experimentally observed 2100 cm^{-1} peak thus justifying the absence of the 2020 cm^{-1} peak.

Indeed, Ni particles doped with Mn may show a higher affinity toward oxidation because oxygen chemisorbs stronger to $NiMn_x$ than Ni. In particular, the O* binding energies on pristine Ni(100) and $NiMn_x$(100), calculated analogously to Eq. (2), are −5.3 and −5.6 eV, respectively. This result, therefore, corroborates the hypothesis that the absence of 2020 cm^{-1} peak of the Ni/Mn_xCeO_2 catalyst is due to the higher oxidation of metal particles compared to those on CeO_2.

3.3. Reaction mechanisms

To evaluate the explanation that emerged from the above vibrational analysis, which ascribes the absence of the 2020 cm^{-1} peak to oxidized Ni particles, the DRM reaction mechanism was explored on Ni(111) and NiO(100).

Two reaction paths were considered for the dissociation of methane (CH_4). The first is the direct dissociation via the C–H bond cleavages and the second is an indirect one, which proceeds via the formation of the CH_xO species. For the CO_2 dissociation, three different reaction paths were explored: direct dissociation to CO + O and indirect paths through the formation of carboxylic (COOH) and formate (HCOO) species.

Structures of the initial and final states corresponding to meaningful stable structures were used in NEB calculations. Some reactions consist of two elementary steps, one representing the movement of a molecule and the other the intramolecular bond-breaking or making. The molecular movement was considered in cases with a relevant energy difference between the most stable structure and the structure used in calculating intramolecular bond-making or breaking. This approach provides a more realistic assessment of reaction energies.

Note that the energies of adsorbed species depend on the coverage and presence of other coadsorbed species [70]; these issues are addressed at the end of the manuscript. For this reason, the presented reaction and activation energies are to be taken qualitatively only.

3.3.1. Ni(111)

All tested elementary reaction steps for CH_4 and CO_2 decomposition on Ni(111) and their corresponding reaction and activation energies are shown in Fig. 1. The reaction paths that involve the elementary steps with the lowest activation barriers are highlighted with green color and their reaction energy profiles are shown in Fig. 2.

The first abstraction of the H atom from methane has a high activation barrier of 0.99 eV, but the two subsequent steps leading to the CH* fragment have lower barriers (0.75 and 0.35 eV). The abstraction of the last H atom, CH* ⟶ C* + H*, displays the highest H-abstraction activation energy of 1.31 eV. The activation energy for the oxidation of C* to CO* is very high (2.11 eV), which is in line with the fact that adsorbed carbon acts as a poison for the catalyst. Hence, the formation of CO instead follows the path through the CHO* fragment, i.e., CH* + O* ⟶ CHO* ⟶ CO* + H* with the respective activation energies of 1.15 and 0.18 eV. Although the activation barrier for the CH* + O* ⟶ CHO* step is slightly lower than the barrier for the CH* ⟶ C* + H* alternative, C* may eventually form as a byproduct of the reaction due to the small difference between the two barriers. Another possibility that leads to CO* is the reaction of CH_2* with O* that has a slightly lower activation energy (1.05 eV) than the CH* + O* reaction (1.15 eV), but the barrier for the dissociation of CH_2* to CH* is considerably lower (0.35 eV), making the oxidation of CH_2* less likely. These results imply that the CO* formation from methane proceeds first by H-abstraction until CH* is formed, which then oxidizes to CHO* and CHO* subsequently dissociates to CO*.

The second group of reactions pertains to CO_2 decomposition. CO_2 can adsorb in two modes, a weakly bound physisorbed mode (E_{ads} = −0.03 eV) and an activated V-shaped chemisorbed CO_2* structure, for which the adsorption energy is endothermic (E_{ads} = +0.36 eV);[4] this V-shaped structure is metastable because it is a shallow local minimum on the potential-energy surface (PES) but is needed for the reaction to proceed. According to our calculations, the next step is a direct dissociation to CO* and O*, which displays lower activation energy (0.52 eV) than the formation of HCOO* (0.57 eV) and COOH* (0.84 eV) intermediates. Oxygen atoms formed in the CO_2 dissociation are used in reactions with CH_2* and CH* fragments to produce CH_2O* and CHO* which subsequently dissociate to CO*.

The activation barriers for reactions involving the H* and O* intermediates were also calculated. The associative formation of hydrogen, 2H* ⟶ H_2*, has an activation barrier of 0.92 eV. For water formation, the calculated activation energies are 1.05 eV for the O* + H* ⟶ OH* step and 1.27 eV for the subsequent H* + OH* ⟶ H_2O* step, implying that the H_2 formation is faster than the formation of H_2O on metallic Ni surfaces.

The above DFT results indicate that metallic Ni is a viable DRM catalyst because it can lead to both products of the DRM reaction, CO and H_2. Considering the most probable reaction paths on Ni(111), colored green in Fig. 1, the involved elementary reaction steps with the highest activation energies are the first H-abstraction from methane,

[3] The mixing energy was calculated as:

$$E_{mix} = \frac{1}{m}(E_{NiMn_x} - nE_{Ni} - mE_{Mn}),$$

where E_{NiMn_x} is the energy of the $NiMn_x$ bulk alloy supercell consisting of n Ni and m Mn atoms. E_{Ni} and E_{Mn} are the energies of Ni and Mn atoms in the respective bulk crystals. The so-calculated mixing energy is normalized per Mn atom. The fcc lattice of Ni was used for the starting structure of the $NiMn_x$ alloy, which was further relaxed with variable cell optimization. As for the bulk Mn, a plain bcc lattice was used for simplicity, although α-Mn has a unique bcc lattice with 58 atoms in the unit cell [69].

[4] The PBE-D3 functional, which includes the dispersion correction [71], gives the E_{ads} values of −0.23 and +0.1 eV for physisorbed CO_2 and the V-shaped chemisorbed state, respectively.

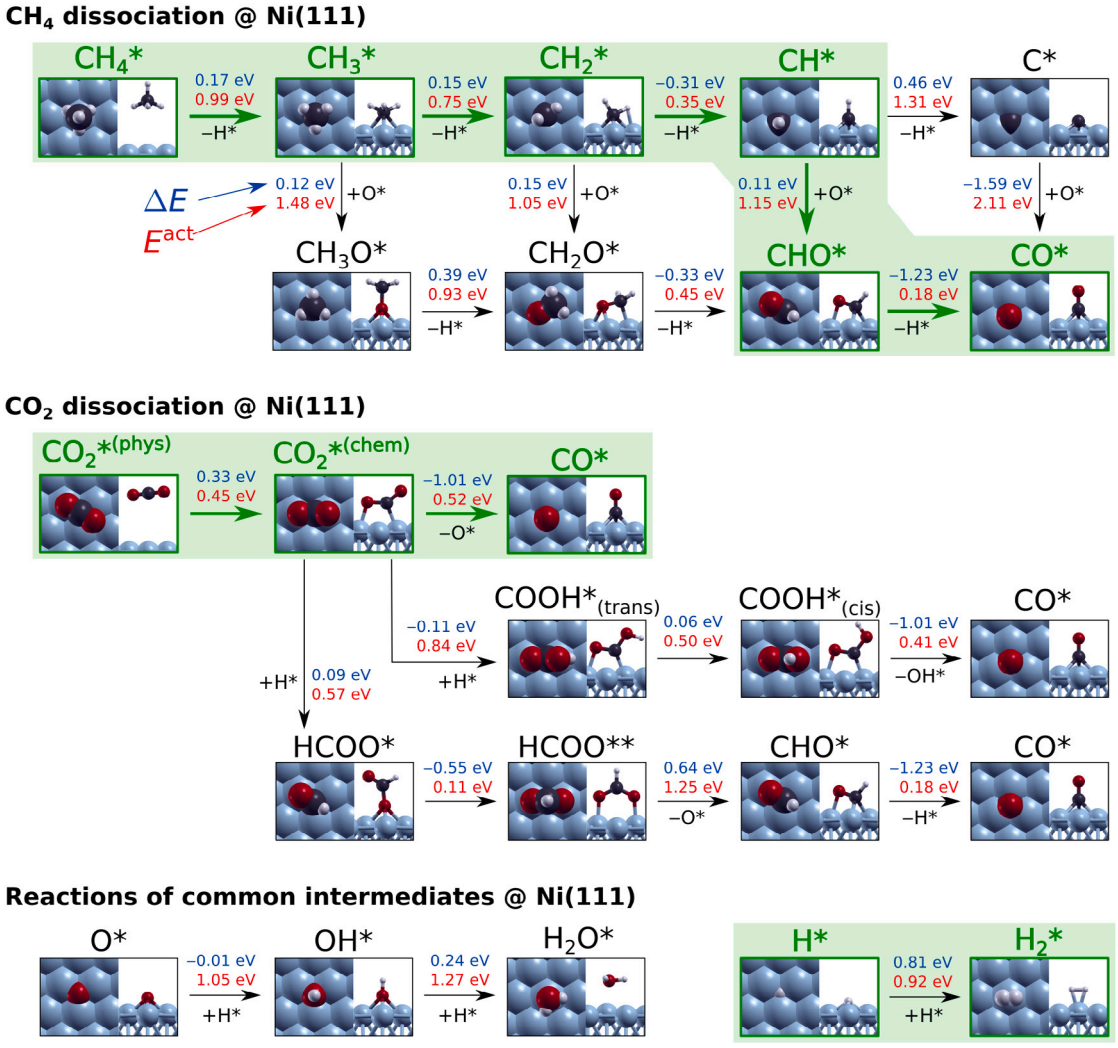

Fig. 1. Snapshots and the calculated reaction (ΔE, blue) and activation (E^{act}, red) energies of the reaction elementary steps on Ni(111), involved in the decomposition of CH_4 and CO_2 as well as the formation of water and hydrogen molecules. The reaction paths involving the elementary steps with the lowest activation barriers are highlighted in green for each reaction. All calculated reaction energy paths and the corresponding IS, TS, and FS structures are shown in Figs. S5–S26 in the Supplementary material.

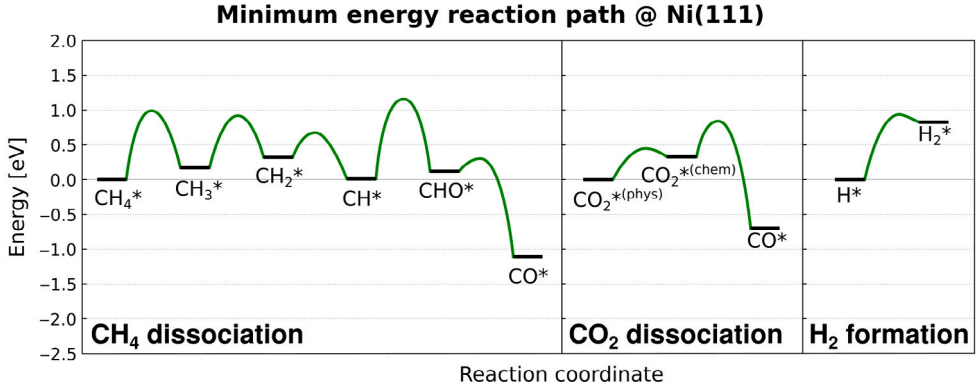

Fig. 2. The reaction energy profiles for reaction paths with the lowest energy barriers on Ni(111), i.e., the green colored reaction paths in Fig. 1.

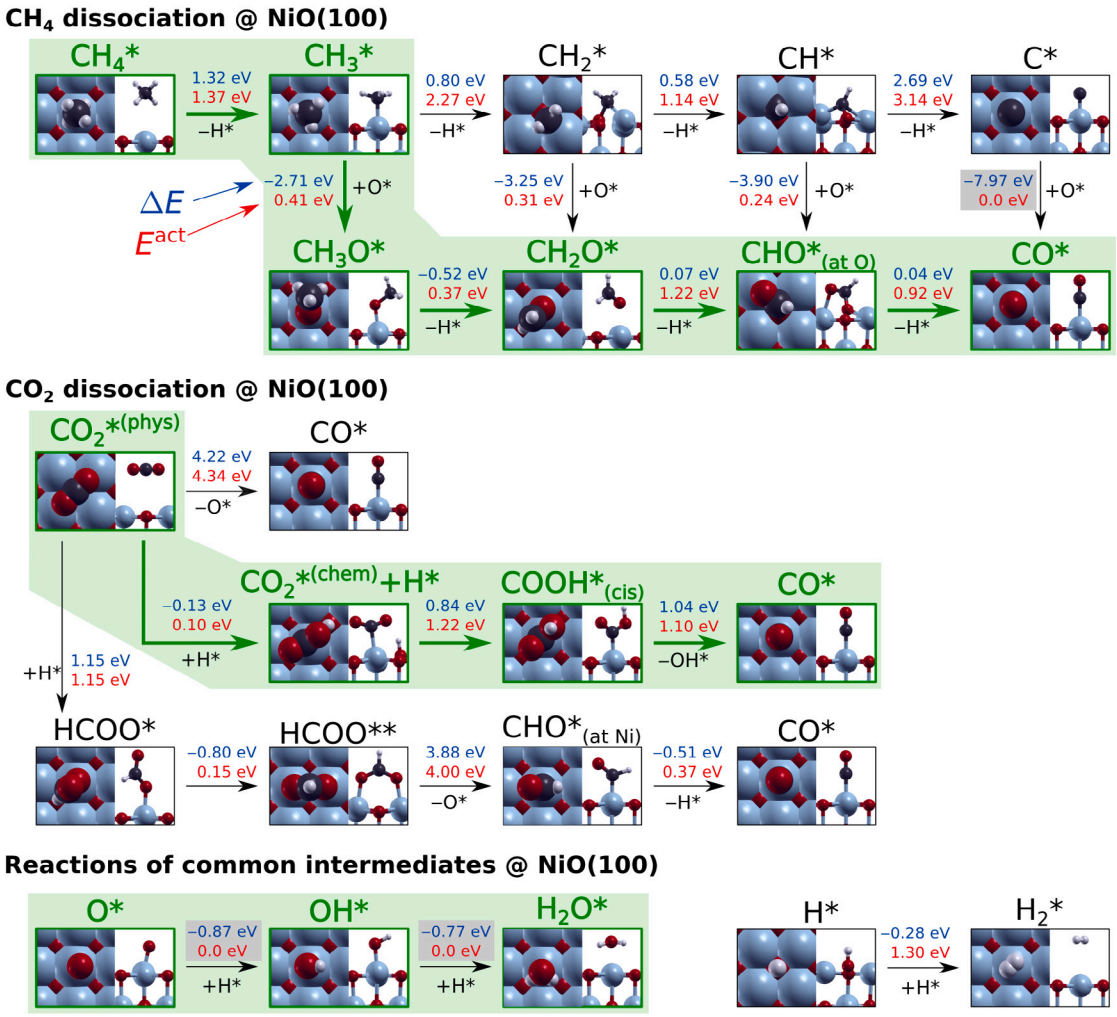

Fig. 3. Similar to Fig. 1, but for reactions on NiO(100). The reaction paths involving the elementary steps with the lowest activation barriers are highlighted in green for each reaction. The gray-shaded ΔE values were calculated with constrained relaxations of co-adsorbed reactants because full relaxation of co-adsorbed reactants resulted in the product; such reactions are barrierless ($E^{act} = 0$ eV). All calculated reaction energy paths and the corresponding IS, TS, and FS structures are shown in Figs. S27–S45 in the Supplementary material.

reaction of CH* with O*, and the formation of H_2. One problem with Ni catalysts is that the activation barrier for the C* formation is not considerably higher from the competing reactions that lead to the DRM products. Therefore, C* eventually poisons the surface, making the catalyst inactive.

3.3.2. NiO(100)

The considered reaction paths on NiO(100) are shown in Fig. 3; they are analogous to those examined above on Ni(111). As for the methane H-abstraction reactions on NiO(100), the first abstraction displays a higher activation energy (1.37 eV) than on Ni(111) (0.99 eV). The subsequent $CH_3^* \longrightarrow CH_2 + H^*$ step displays exceedingly high activation energy of 2.27 eV. Hence, the reaction proceeds through the CH_xO intermediates because the $CH_x^* + O^*$ reactions are highly exothermic and display rather small activation energies of 0.41, 0.31, and 0.24 eV for $x = 3$, 2, and 1, respectively.

Due to the exceedingly high activation barrier of the $CH^* \longrightarrow C^* + H^*$ reaction (3.14 eV), the formation of C* in unfeasible on NiO(100). Furthermore, the $C^* + O^* \longrightarrow CO^*$ reaction is highly exothermic and barrier-less, further corroborating the unfeasibility of the C* accumulation and subsequent surface poisoning on NiO(100). However, the $CH_x^* + O^*$ oxidation reactions require excess O* species on NiO(100), yet our results indicate that their formation is unlikely on NiO(100) (see below). Hence, O* can either form on reduced Ni patches or originate from the ceria support.

As for reactions involving CO_2, a direct dissociation of CO_2^* to CO* + O* can be excluded on NiO(100) due to extremely high activation energy and highly endothermic reaction ($\Delta E > 4$ eV). The reaction instead proceeds via the V-shaped chemisorbed CO_2^* that is stabilized by the nearby H*, which first transforms to a cis-carboxylic COOH* species ($E^{act} = 1.22$ eV) and then decomposes to CO* + OH* ($E^{act} = 1.10$ eV). Here, it should be noted that the formation of the formate HCOO* intermediate displays a slightly lower activation barrier (1.15 eV) than the formation of the carboxylic COOH* species (1.22 eV). However, the formation of the formate is a dead end because it cannot decompose to CHO* ($E^{act} = 4.0$ eV) that would lead to CO*.

It is a notable observation that O* species cannot form on NiO(100) because CO_2^* and CO* dissociations are both extremely endothermic thereon (Fig. 3). Furthermore, even if O* would form on NiO(100), it would react barrierlessly with nearby H* atoms, exothermally forming water molecules. The associative formation of hydrogen, $2H^* \longrightarrow H_2^*$, is also exothermic ($\Delta E = -0.28$ eV), but displays a sizable activation energy of 1.30 eV, which is higher than on Ni(111), 0.92 eV.

The current results show that, on the one hand, NiO by itself cannot act as a catalyst because the decomposition of methane either requires the presence of excess O* species, which is unlikely on NiO, or the reaction path that omit the O* species displays too high activation

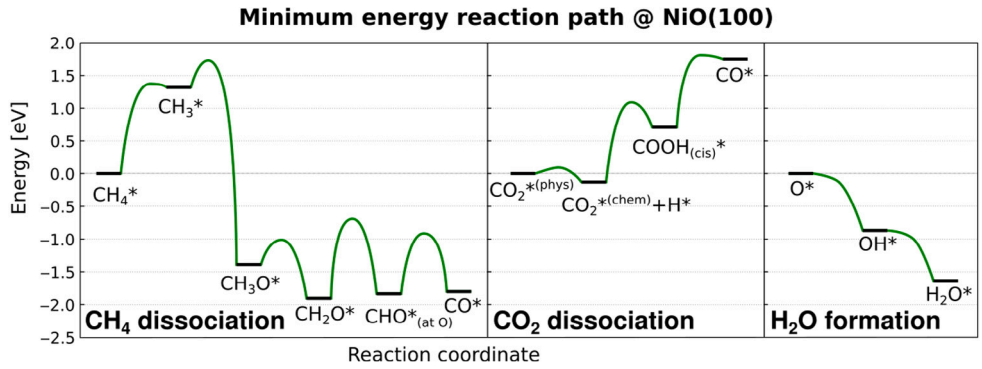

Fig. 4. The reaction energy profiles for reaction paths with the lowest energy barriers on NiO(100), i.e., the green colored reaction paths in Fig. 3.

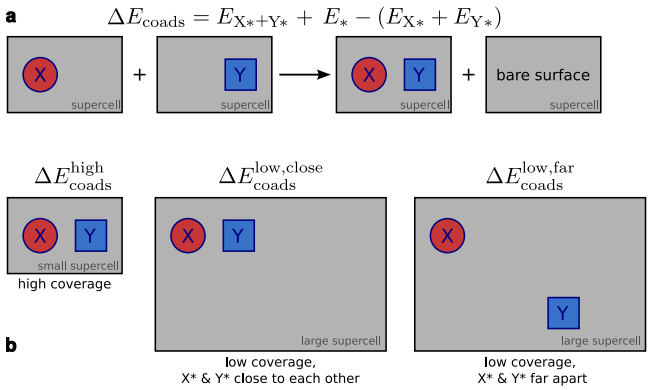

Fig. 5. Schematic presentation of how the coadsorption effects were estimated. (a) Schematic of the ΔE_{coads} calculation. (b) To scrutinize the effects of the coverage and the intermolecular distance on the X* + Y* relative stability, the ΔE_{coads} values were calculated with smaller and larger supercells with coadsorbates close to each other and far apart.

energies for some elementary steps (i.e., for $CH_3^* \longrightarrow CH_2^* + H^*$ and $CH^* \longrightarrow C^* + H^*$). On the other hand, the coke formation is not expected on NiO, which is a plus. This observation suggests that partially oxidized Ni should be superior to both metallic Ni and fully oxidized NiO because, by a simple extrapolation, partially oxidized Ni should display lower affinity to coke formation than metallic Ni but higher viability of the DRM reaction than fully oxidized NiO. The viability of the DRM reaction on partially oxidized Ni nanoparticles should be even higher on supports that could provide O* species such as currently used CeO_2 and Mn_xCeO_2.

3.4. Coadsorption effects

As already mentioned above, the reaction and activation energies presented in Figs. 1–4 are to be taken qualitatively because they were calculated at a specific computational "setup" without exploring coverage and coadsorption effects. To shed some light onto these issues, we present below a simplified attempt at estimating how various coadsorbed species affect thermodynamic stability of each other.

The reactions considered in Figs. 1 and 3 are either dissociations ($XY^* \longrightarrow X^* + Y^*$) or associations ($X^* + Y^* \longrightarrow XY^*$) and the majority of them involve either H* or O* as one of the product or reactant; hence, Y* is either O* or H*, whereas X* is any of the species considered in Figs. 1 and 3. In NEB calculations, the reaction and activation energies are calculated using a single supercell for the whole reaction, implying that surface coverage changes during a reaction because one adsorbate per supercell (XY*) transforms into two coadsorbates per supercell (X* + Y*) or vice-versa. The coadsorption effect (ΔE_{coads}) on the adsorption energy was therefore estimated by considering the coadsorbed X* + Y* configuration in a given supercell to the standalone X* and Y* configurations in the same supercell (for the schematic representation of ΔE_{coads}, see Fig. 5a), i.e.:

$$\Delta E_{coads} = E_{X*+Y*} + E_* - (E_{X*} + E_{Y*}), \quad (5)$$

where E_{X*+Y*} is the energy of the coadsorbed X* + Y* configuration, E_* is the energy of the bare surface, while E_{X*} and E_{Y*} are the energies of the standalone X* and Y* configurations; all these energies were calculated with the same supercell. The corresponding results are presented in Table S3 in the Supplementary material.

3.4.1. Ni(111)

According to the results of Table S3, H* only marginally affects the adsorption energies of coadsorbed species on Ni(111) because the ΔE_{coads} magnitudes are below 0.1 eV. In contrast, the effect of O* is somewhat larger but still relatively small, $\Delta E_{coads} \leq 0.25$ eV. All ΔE_{coads} values are positive, indicating that H* and O* tend to slightly destabilize the coadsorbed species. However, the energy differences are relatively minor; hence, the above-discussed reaction mechanisms on Ni(111) are valid, and the presented reaction and activation energies are reliable.

3.4.2. NiO(100)

The coadsorption effects on NiO(100) are much greater than on Ni(111), and all the considered coadsorbed structures are stabilized compared to the singly-adsorbed species (Table S3). H* stabilizes the coadsorbed species from about 0.5 to 1.1 eV; for H* + O* and H* + OH*, the stabilization is even much stronger (1.7 and 1.9 eV), but in these cases the coadsorbed structures at neighboring sites are not stable and barrierlessly transform to OH* and H_2O*, respectively. In contrast, O* has either a marginal effect ($|\Delta E_{coads}| < 0.1$ eV) or a super strong effect ($|\Delta E_{coads}| \gtrsim 1.2$ eV). The marginal effect appears only for structures with both X* and Y* species bonded to Ni ions. In contrast, when at least one of the coadsorbed species bind to a surface O ion, then the O* coadsorption effect is strong.

The coadsorption effects on NiO(100) are therefore sizable for most considered cases, suggesting that the reaction and activation energies are highly susceptible to the surface coverage and the distance between the reacting coadsorbates (we call the latter the "closeness effect"). This case thus needs further scrutiny to determine the reliability of the calculated reaction and activation energies of Fig. 3. The first relevant observation is that for association reactions, the two involved species must be coadsorbed close to each other to react. Likewise, for dissociation reactions the two emerging species are coadsorbed close to each other immediately after the bond cleavage. This implies that coadsorbed configurations with X* and Y* close to each other are more relevant for activation energies than standalone adsorbed configurations. However, configurations with X* and Y* close to each other can be considered at different coverages. To estimate the effects of closeness and coverage, we performed ΔE_{coads} calculations with three NiO(100)

supercells of increasing size: (2 × 2), (4 × 2), and (4 × 4). For larger supercells, X* and Y* coadsorbates were considered close to each other (named as "close" configurations) and also further apart (designated as "far"). This approach is schematically presented in Fig. 5b.

The so-calculated ΔE_{coads} are presented in Table S4 for three coadsorption pairs: H* + CH_3*, H* + CH_2*, and O* + CH_2* (the snapshots of the considered configurations are presented in Fig. S4). For the H* + CH_3* and O* + CH_2* coadsorption pairs, the results reveal that the coadsorption effect persists with decreasing coverage because, for the large (4 × 4) supercell, the coadsorption effect is still considerable, particularly if the two coadsorbates are located close to each other. For example, for H* + CH_3*, the ΔE_{coads} values are −0.72, −0.63, and −0.34 eV for (2 × 2), close-(4 × 4), and far-(4 × 4) configurations. These numbers suggest that the close distance between the coadsorbates affects ΔE_{coads} to a larger extent than the coverage.

In contrast, for H* + CH_2*, the coadsorption effect diminishes much faster with decreasing coverage for both close and far configurations. For the small (2×2) supercell, the ΔE_{coads} effect is considerable (−0.81 eV), but for the large (4 × 4) supercell, it is quite small, being −0.02 and 0.04 eV for the close and far configurations, respectively.

These three coadsorption cases reveal that the ΔE_{coads} effect can be either short- or long-ranged. For the long-ranged instances, the calculated E^{act} values of Fig. 3 should be rather insensitive to coverage and thus reliable. In contrast, for the short-ranged case, the calculated E^{act} values are coverage dependent and thus less general or reliable. For the short-ranged cases, the dependence of E^{act} on the coverage can be anticipated with the Brønsted-Evans-Polanyi (BEP) relation [72]. For dissociation reactions (XY* ⟶ X* + Y*), stabilizing the X* + Y* structure proportionally lowers E^{act}, particularly if TS is FS-like. In contrast, for association reactions (X* + Y* ⟶ XY*), stabilizing the X* + Y* structure affects E^{act} to a lesser extent, particularly if TS is IS-like. These arguments imply that, for the dissociation reactions, the E^{act} values reported in Fig. 3 may be considered as lower-bounds because they were calculated with relatively small supercells.

3.5. Diffusion of H* and O*

Because most of the reactions, considered in Figs. 1 and 3, involve either H* or O*, we also calculated the barriers for H* and O* diffusion on Ni(111) and NiO(100). The diffusion barriers on Ni(111) were estimated as the energy difference between a less stable bridge and the most stable fcc site because, according to calculations, the H* and O* diffusion on Ni(111) follows the fcc⟶bridge⟶hcp⟶bridge⟶fcc path.[5] The calculations reveal that H* is considerably more mobile on Ni(111) than O* because the estimated diffusion barriers are 0.1 and 0.5 eV, respectively. The two barriers are sufficiently small to allow efficient diffusion at reaction temperatures.

On NiO(100), the H* and O* diffusion barriers were calculated with CI-NEB. The so-calculated H* diffusion barrier is 0.9 eV, which is considerably higher than on Ni(111). In contrast, the O* diffusion barrier is about 0.5 eV thus being similar as on Ni(111). O* is therefore more mobile and more likely to react with intermediates than H*, making the H_2 formation compared to the water formation even less likely on NiO(100).

4. Conclusion

To explain the experimentally observed difference between the Ni/CeO_2 and Ni/Mn_xCeO_2 catalysts for the DRM reaction, specifically the absence of the 2020 cm^{-1} vibrational peak on Ni/Mn_xCeO_2, we performed a computational DFT study of the DRM reaction on Ni catalysts, using different Ni catalyst models, i.e., low Miller index Ni surfaces as models of metallic Ni particles (pristine and doped with Mn), NiO(100) as a model of fully oxidized Ni particles, and O/Ni(100) and $O/NiMn_x$(100) as simple models of partially oxidized metal particles.

Computational vibrational analysis univocally attributes the experimentally observed 2020 cm^{-1} peak to the CO stretching vibration of CO adsorbed on a top site of metallic Ni because all other sites and involved species display considerably different frequencies. The CO stretching frequency increases as Ni oxidizes, and on NiO(100), it is similar to the frequency of CO vibration on CeO_2(111), about 2100 cm^{-1}. This observation suggests that Ni particles supported on Mn_xCeO_2 are more oxidized than those on CeO_2 so that only the latter catalyst displays sufficiently metallic Ni particles for the 2020 cm^{-1} peak to appear. This hypothesis is supported by calculations, which reveal that Mn doping of Ni particles should enhance oxidation due to a stronger metal–O interaction in the presence of Mn.

To substantiate the hypothesis of varying degrees of oxidation of Ni nanoparticles on the two catalysts, we investigated the DRM reaction mechanism on Ni(111) and NiO(100) as models of fully reduced and fully oxidized Ni, respectively. The reaction-path calculations reveal that DRM on metallic Ni is feasible at elevated temperatures. According to calculations, the reaction proceeds by H-abstraction from methane until CH* is formed, which reacts with O* forming CHO*, and CHO* then dissociates to CO*. The H* atoms formed during these H-abstractions then recombine to H_2. CO_2 directly dissociates to CO* and O*, providing O* for the oxidation of CH*. However, a notable problem with metallic Ni catalysts is that the activation barrier for the C* formation is not considerably higher from the competing reactions that lead to the DRM products. Therefore, C* eventually poisons the surface, making the catalyst less active (or even inactive). In contrast, NiO does not encounter issues with the C* formation, but it is not an effective catalyst due to too high activation energies, slow surface diffusion of H*, and a shortage of excess O* that is required for oxidation reactions. These two findings suggest that partly oxidized Ni should be a better catalyst because it combines the good features of metallic Ni (low enough activation energies) and fully oxidized Ni (reduced coke formation).

Current results thus provide a sound explanation of why Ni/Mn_xCeO_2 is a superior catalyst to Ni/CeO_2 for the DRM reaction. In particular, the presence of the 2020 cm^{-1} peak on the Ni/CeO_2 catalyst signals that Ni particles are sufficiently metallic and thus susceptible to carbon poisoning. In contrast, the absence of the 2020 cm^{-1} peak on the Ni/Mn_xCeO_2 catalyst indicates that Ni particles are oxidized, i.e., the Ni oxidation is low enough to allow the DRM reaction but high enough to reduce the catalyst's carbon poisoning.

CRediT authorship contribution statement

Lea Gašparič: Conceptualization, Formal analysis, Investigation, Methodology, Visualization, Writing – original draft, Writing – review & editing, Data curation. **Albin Pintar:** Funding acquisition, Project administration, Writing – review & editing. **Anton Kokalj:** Conceptualization, Investigation, Project administration, Supervision, Writing – original draft, Writing – review & editing.

Declaration of competing interest

The authors declare that they have no known competing financial interests or personal relationships that could have appeared to influence the work reported in this paper.

Data availability

Data will be made available on request.

[5] The so-estimated diffusion barriers represent the lower-bound because the diffusion barriers calculated with NEB would be somewhat higher if the bridge site is a local minimum.

Acknowledgments

This work has been financially supported by the Slovenian Research and Innovation Agency (Grant Nos. J7-9401, J7-3151, and P2-0393).

Appendix A. Supplementary data

Supplementary material related to this article can be found online at https://doi.org/10.1016/j.apsusc.2023.159029.

References

[1] V.T. Sagar, A. Pintar, Enhanced surface properties of CeO_2 by MnO_x doping and their role in mechanism of methane dry reforming deduced by means of in-situ DRIFTS, Appl. Catal. A 599 (2020) 117603, http://dx.doi.org/10.1016/j.apcata.2020.117603.

[2] D.R. Lide (Ed.), CRC Handbook of Chemistry and Physics, 85th ed., CRC Press, Boca Raton, Florida USA, 2005.

[3] M. Rezaei, S.M. Alavi, S. Sahebdelfar, P. Bai, X. Liu, Z.-F. Yan, CO_2 reforming of CH_4 over nanocrystalline zirconia-supported nickel catalysts, Appl. Catal. B 77 (3) (2008) 346–354, http://dx.doi.org/10.1016/j.apcatb.2007.08.004.

[4] I.V. Yentekakis, P. Panagiotopoulou, G. Artemakis, A review of recent efforts to promote dry reforming of methane (DRM) to syngas production via bimetallic catalyst formulations, Appl. Catal. B 296 (2021) 120210, http://dx.doi.org/10.1016/j.apcatb.2021.120210.

[5] M. Jafarbegloo, A. Tarlani, A.W. Mesbah, S. Sahebdelfar, Thermodynamic analysis of carbon dioxide reforming of methane and its practical relevance, Int. J. Hydrog. Energy 40 (6) (2015) 2445–2451, http://dx.doi.org/10.1016/j.ijhydene.2014.12.103.

[6] W.-J. Jang, D.-W. Jeong, J.-O. Shim, H.-M. Kim, H.-S. Roh, I.H. Son, S.J. Lee, Combined steam and carbon dioxide reforming of methane and side reactions: Thermodynamic equilibrium analysis and experimental application, Appl. Energy 173 (2016) 80–91, http://dx.doi.org/10.1016/j.apenergy.2016.04.006.

[7] N.A.K. Aramouni, J.G. Touma, B.A. Tarboush, J. Zeaiter, M.N. Ahmad, Catalyst design for dry reforming of methane: Analysis review, Renew. Sustain. Energy Rev. 82 (2018) 2570–2585, http://dx.doi.org/10.1016/j.rser.2017.09.076.

[8] J.J. Torrez-Herrera, S.A. Korili, A. Gil, Recent progress in the application of Ni-based catalysts for the dry reforming of methane, Catal. Rev. (2021) 1–58, http://dx.doi.org/10.1080/01614940.2021.2006891.

[9] L.P. Teh, H.D. Setiabudi, S.N. Timmiati, M.A.A. Aziz, N.H.R. Annuar, N.N. Ruslan, Recent progress in ceria-based catalysts for the dry reforming of methane: A review, Chem. Eng. Sci. 242 (2021) 116606, http://dx.doi.org/10.1016/j.ces.2021.116606.

[10] F.d.A.R. da Silva, R.C.R. dos Santos, R.S. Nunes, A. Valentini, Role of tin on the electronic properties of Ni/Al_2O_3 catalyst and its effect over the methane dry reforming reaction, Appl. Catal. A 618 (2021) 118129, http://dx.doi.org/10.1016/j.apcata.2021.118129.

[11] J. Liu, H. Peng, W. Liu, X. Xu, X. Wang, C. Li, W. Zhou, P. Yuan, X. Chen, W. Zhang, H. Zhan, Tin modification on Ni/Al_2O_3: Designing potent coke-resistant catalysts for the dry reforming of methane, ChemCatChem 6 (7) (2014) 2095–2104, http://dx.doi.org/10.1002/cctc.201402091.

[12] W. Liu, L. Li, S. Lin, Y. Luo, Z. Bao, Y. Mao, K. Li, D. Wu, H. Peng, Confined Ni-In intermetallic alloy nanocatalyst with excellent coking resistance for methane dry reforming, J. Energy Chem. 65 (2022) 34–47, http://dx.doi.org/10.1016/j.jechem.2021.05.017.

[13] Z. Bian, S. Kawi, Highly carbon-resistant $Ni–Co/SiO_2$ catalysts derived from phyllosilicates for dry reforming of methane, J. CO2 Util. 18 (2017) 345–352, http://dx.doi.org/10.1016/j.jcou.2016.12.014.

[14] S.A. Theofanidis, V.V. Galvita, H. Poelman, G.B. Marin, Enhanced carbon-resistant dry reforming Fe-Ni catalyst: Role of Fe, ACS Catal. 5 (5) (2015) 3028–3039, http://dx.doi.org/10.1021/acscatal.5b00357.

[15] C. Pizzolitto, E. Pupulin, F. Menegazzo, E. Ghedini, A. Di Michele, M. Mattarelli, G. Cruciani, M. Signoretto, Nickel based catalysts for methane dry reforming: Effect of supports on catalytic activity and stability, Int. J. Hydrog. Energy 44 (52) (2019) 28065–28076, http://dx.doi.org/10.1016/j.ijhydene.2019.09.050.

[16] I. Iglesias, G. Baronetti, F. Mariño, $Ni/Ce_{0.95}M_{0.05}O_{2-d}$ (M=Zr, Pr, La) for methane steam reforming at mild conditions, Int. J. Hydrog. Energy 42 (50) (2017) 29735–29744, http://dx.doi.org/10.1016/j.ijhydene.2017.09.176.

[17] A. Löfberg, J. Guerrero-Caballero, T. Kane, A. Rubbens, L. Jalowiecki-Duhamel, Ni/CeO_2 based catalysts as oxygen vectors for the chemical looping dry reforming of methane for syngas production, Appl. Catal. B 212 (2017) 159–174, http://dx.doi.org/10.1016/j.apcatb.2017.04.048.

[18] A.L.A. Marinho, R.C. Rabelo-Neto, F. Epron, N. Bion, F.S. Toniolo, F.B. Noronha, Embedded Ni nanoparticles in $CeZrO_2$ as stable catalyst for dry reforming of methane, Appl. Catal. B 268 (2020) 118387, http://dx.doi.org/10.1016/j.apcatb.2019.118387.

[19] Ş. Özkara-Aydınoğlu, Thermodynamic equilibrium analysis of combined carbon dioxide reforming with steam reforming of methane to synthesis gas, Int. J. Hydrog. Energy 35 (23) (2010) 12821–12828, http://dx.doi.org/10.1016/j.ijhydene.2010.08.134.

[20] Y. Li, Y. Wang, X. Zhang, Z. Mi, Thermodynamic analysis of autothermal steam and CO_2 reforming of methane, Int. J. Hydrog. Energy 33 (10) (2008) 2507–2514, http://dx.doi.org/10.1016/j.ijhydene.2008.02.051.

[21] C. Jensen, M.S. Duyar, Thermodynamic analysis of dry reforming of methane for valorization of landfill gas and natural gas, Energy Technol. 9 (7) (2021) 2100106, http://dx.doi.org/10.1002/ente.202100106.

[22] H. Atashi, J. Gholizadeh, F. Farshchi Tabrizi, J. Tayebi, S.A.H. Seyed Mousavi, Thermodynamic analysis of carbon dioxide reforming of methane to syngas with statistical methods, Int. J. Hydrog. Energy 42 (8) (2017) 5464–5471, http://dx.doi.org/10.1016/j.ijhydene.2016.07.184.

[23] V.R. Bach, A.C. de Camargo, T.L. de Souza, L. Cardozo-Filho, H.J. Alves, Dry reforming of methane over $Ni/MgO–Al_2O_3$ catalysts: Thermodynamic equilibrium analysis and experimental application, Int. J. Hydrog. Energy 45 (8) (2020) 5252–5263, http://dx.doi.org/10.1016/j.ijhydene.2019.07.200.

[24] S. Chen, J. Zaffran, B. Yang, Dry reforming of methane over the cobalt catalyst: Theoretical insights into the reaction kinetics and mechanism for catalyst deactivation, Appl. Catal. B 270 (2020) 118859, http://dx.doi.org/10.1016/j.apcatb.2020.118859.

[25] O. Mohan, Shambhawi, A.A. Lapkin, S.H. Mushrif, Investigating methane dry reforming on Ni and B promoted Ni surfaces: DFT assisted microkinetic analysis and addressing the coking problem, Catal. Sci. Technol. 10 (19) (2020) 6628–6643, http://dx.doi.org/10.1039/D0CY00939C.

[26] C. Fan, Y.-A. Zhu, M.-L. Yang, Z.-J. Sui, X.-G. Zhou, D. Chen, Density functional theory-assisted microkinetic analysis of methane dry reforming on Ni catalyst, Ind. Eng. Chem. Res. 54 (22) (2015) 5901–5913, http://dx.doi.org/10.1021/acs.iecr.5b00563.

[27] S.-G. Wang, D.-B. Cao, Y.-W. Li, J. Wang, H. Jiao, CO_2 reforming of CH_4 on Ni(111): A density functional theory calculation, J. Phys. Chem. B 110 (20) (2006) 9976–9983, http://dx.doi.org/10.1021/jp060992g.

[28] Z. Han, Z. Yang, M. Han, Comprehensive investigation of methane conversion over Ni(111) surface under a consistent DFT framework: Implications for anti-coking of SOFC anodes, Appl. Surf. Sci. 480 (2019) 243–255, http://dx.doi.org/10.1016/j.apsusc.2019.02.084.

[29] S.-G. Wang, X.-Y. Liao, J. Hu, D.-B. Cao, Y.-W. Li, J. Wang, H. Jiao, Kinetic aspect of CO_2 reforming of CH_4 on Ni(111): A density functional theory calculation, Surf. Sci. 601 (5) (2007) 1271–1284, http://dx.doi.org/10.1016/j.susc.2006.12.059.

[30] S.-G. Wang, D.-B. Cao, Y.-W. Li, J. Wang, H. Jiao, Reactivity of surface OH in CH_4 reforming reactions on Ni(111): A density functional theory calculation, Surf. Sci. 603 (16) (2009) 2600–2606, http://dx.doi.org/10.1016/j.susc.2009.06.009.

[31] M. Zhang, K. Yang, X. Zhang, Y. Yu, Effect of Ni(111) surface alloying by Pt on partial oxidation of methane to syngas: A DFT study, Surf. Sci. 630 (2014) 236–243, http://dx.doi.org/10.1016/j.susc.2014.08.023.

[32] S. Kawi, Y. Kathiraser, J. Ni, U. Oemar, Z. Li, E.T. Saw, Progress in synthesis of highly active and stable nickel-based catalysts for carbon dioxide reforming of methane, ChemSusChem 8 (21) (2015) 3556–3575, http://dx.doi.org/10.1002/cssc.201500390.

[33] P.M. Mortensen, I. Dybkjær, Industrial scale experience on steam reforming of CO_2-rich gas, Appl. Catal. A 495 (2015) 141–151, http://dx.doi.org/10.1016/j.apcata.2015.02.022.

[34] P.A.U. Aldana, F. Ocampo, K. Kobl, B. Louis, F. Thibault-Starzyk, M. Daturi, P. Bazin, S. Thomas, A.C. Roger, Catalytic CO_2 valorization into CH_4 on Ni-based ceria-zirconia. Reaction mechanism by operando IR spectroscopy, Catal. Today 215 (2013) 201–207, http://dx.doi.org/10.1016/j.cattod.2013.02.019.

[35] X. Li, D. Li, H. Tian, L. Zeng, Z.-J. Zhao, J. Gong, Dry reforming of methane over Ni/La_2O_3 nanorod catalysts with stabilized Ni nanoparticles, Appl. Catal. B 202 (2017) 683–694, http://dx.doi.org/10.1016/j.apcatb.2016.09.071.

[36] J. Carrasco, L. Barrio, P. Liu, J.A. Rodriguez, M.V. Ganduglia-Pirovano, Theoretical studies of the adsorption of CO and C on Ni(111) and $Ni/CeO_2(111)$: Evidence of a strong metal–support interaction, J. Phys. Chem. C 117 (16) (2013) 8241–8250, http://dx.doi.org/10.1021/jp400430r.

[37] Z. Mao, P.G. Lustemberg, J.R. Rumptz, M.V. Ganduglia-Pirovano, C.T. Campbell, Ni nanoparticles on $CeO_2(111)$: Energetics, electron transfer, and structure by Ni adsorption calorimetry, spectroscopies, and density functional theory, ACS Catal. 10 (9) (2020) 5101–5114, http://dx.doi.org/10.1021/acscatal.0c00333.

[38] P.G. Lustemberg, P.J. Ramírez, Z. Liu, R.A. Gutiérrez, D.G. Grinter, J. Carrasco, S.D. Senanayake, J.A. Rodriguez, M.V. Ganduglia-Pirovano, Room-temperature activation of methane and dry re-forming with CO_2 on $Ni-CeO_2(111)$ surfaces: Effect of Ce^{3+} sites and metal–support interactions on C–H bond cleavage, ACS Catal. 6 (12) (2016) 8184–8191, http://dx.doi.org/10.1021/acscatal.6b02360.

[39] P.G. Lustemberg, R.M. Palomino, R.A. Gutiérrez, D.C. Grinter, M. Vorokhta, Z. Liu, P.J. Ramírez, V. Matolín, M.V. Ganduglia-Pirovano, S.D. Senanayake, J.A. Rodriguez, Direct conversion of methane to methanol on Ni-ceria surfaces: Metal–support interactions and water-enabled catalytic conversion by site blocking, J. Am. Chem. Soc. 140 (24) (2018) 7681–7687, http://dx.doi.org/10.1021/jacs.8b03809.

[40] K. Yuan, J.-Q. Zhong, X. Zhou, L. Xu, S.L. Bergman, K. Wu, G.Q. Xu, S.L. Bernasek, H.X. Li, W. Chen, Dynamic oxygen on surface: Catalytic intermediate and coking barrier in the modeled CO_2 reforming of CH_4 on Ni(111), ACS Catal. 6 (7) (2016) 4330–4339, http://dx.doi.org/10.1021/acscatal.6b00357.

[41] Z. Wang, X.-M. Cao, J. Zhu, P. Hu, Activity and coke formation of nickel and nickel carbide in dry reforming: A deactivation scheme from density functional theory, J. Catal. 311 (2014) 469–480, http://dx.doi.org/10.1016/j.jcat.2013.12.015.

[42] S. Praserthdam, S. Somdee, M. Rittiruam, P.B. Balbuena, Computational study of the evolution of Ni-based catalysts during the dry reforming of methane, Energy Fuels 34 (4) (2020) 4855–4864, http://dx.doi.org/10.1021/acs.energyfuels.9b04350.

[43] Y.J.O. Asencios, E.M. Assaf, Combination of dry reforming and partial oxidation of methane on NiO–MgO–ZrO_2 catalyst: Effect of nickel content, Fuel Process. Technol. 106 (2013) 247–252, http://dx.doi.org/10.1016/j.fuproc.2012.08.004.

[44] U. Oemar, K. Hidajat, S. Kawi, Role of catalyst support over PdO–NiO catalysts on catalyst activity and stability for oxy-CO_2 reforming of methane, Appl. Catal. A 402 (1) (2011) 176–187, http://dx.doi.org/10.1016/j.apcata.2011.06.002.

[45] S.P. Padi, L. Shelly, E.P. Komarala, D. Schweke, S. Hayun, B.A. Rosen, Coke-free methane dry reforming over nano-sized NiO-CeO_2 solid solution after exsolution, Catal. Commun. 138 (2020) 105951, http://dx.doi.org/10.1016/j.catcom.2020.105951.

[46] J. Titus, T. Roussière, G. Wasserschaff, S. Schunk, A. Milanov, E. Schwab, G. Wagner, O. Oeckler, R. Gläser, Dry reforming of methane with carbon dioxide over NiO–MgO–ZrO_2, Catal. Today 270 (2016) 68–75, http://dx.doi.org/10.1016/j.cattod.2015.09.027.

[47] Y.J.O. Asencios, J.D.A. Bellido, E.M. Assaf, Synthesis of NiO–MgO–ZrO_2 catalysts and their performance in reforming of model biogas, Appl. Catal. A 397 (1) (2011) 138–144, http://dx.doi.org/10.1016/j.apcata.2011.02.023.

[48] P. Giannozzi, S. Baroni, N. Bonini, M. Calandra, R. Car, C. Cavazzoni, D. Ceresoli, G.L. Chiarotti, M. Cococcioni, I. Dabo, A. Dal Corso, S. de Gironcoli, S. Fabris, G. Fratesi, R. Gebauer, U. Gerstmann, C. Gougoussis, A. Kokalj, M. Lazzeri, L. Martin-Samos, N. Marzari, F. Mauri, R. Mazzarello, S. Paolini, A. Pasquarello, L. Paulatto, C. Sbraccia, S. Scandolo, G. Sclauzero, A.P. Seitsonen, A. Smogunov, P. Umari, R.M. Wentzcovitch, QUANTUM ESPRESSO: A modular and open-source software project for quantum simulations of materials, J. Phys.: Condens. Matter 21 (39) (2009) 395502, http://dx.doi.org/10.1088/0953-8984/21/39/395502, Code available from http://www.quantum-espresso.org/.

[49] P. Giannozzi, O. Andreussi, T. Brumme, O. Bunau, M. Buongiorno Nardelli, M. Calandra, R. Car, C. Cavazzoni, D. Ceresoli, M. Cococcioni, N. Colonna, I. Carnimeo, A. Dal Corso, S. de Gironcoli, P. Delugas, R.A. DiStasio Jr., A. Ferretti, A. Floris, G. Fratesi, G. Fugallo, R. Gebauer, U. Gerstmann, F. Giustino, T. Gorni, J. Jia, M. Kawamura, H.-Y. Ko, A. Kokalj, E. Küçükbenli, M. Lazzeri, M. Marsili, N. Marzari, F. Mauri, N.L. Nguyen, H.-V. Nguyen, A. Otero-de-la Roza, L. Paulatto, S. Poncé, D. Rocca, R. Sabatini, B. Santra, M. Schlipf, A.P. Seitsonen, A. Smogunov, I. Timrov, T. Thonhauser, P. Umari, N. Vast, X. Wu, S. Baroni, Advanced capabilities for materials modelling with QUANTUM ESPRESSO, J. Phys.: Condens. Matter 29 (2017) 465901, http://dx.doi.org/10.1088/1361-648X/aa8f79.

[50] J.P. Perdew, K. Burke, M. Ernzerhof, Generalized gradient approximation made simple, Phys. Rev. Lett. 77 (18) (1996) 3865–3868, http://dx.doi.org/10.1103/PhysRevLett.77.3865.

[51] V.I. Anisimov, J. Zaanen, O.K. Andersen, Band theory and Mott insulators: Hubbard *U* instead of Stoner *I*, Phys. Rev. B 44 (3) (1991) 943–954, http://dx.doi.org/10.1103/PhysRevB.44.943.

[52] M. Cococcioni, S. de Gironcoli, Linear response approach to the calculation of the effective interaction parameters in the LDA+U method, Phys. Rev. B 71 (3) (2005) 035105, http://dx.doi.org/10.1103/PhysRevB.71.035105.

[53] I. Timrov, N. Marzari, M. Cococcioni, Hubbard parameters from density-functional perturbation theory, Phys. Rev. B 98 (8) (2018) 085127, http://dx.doi.org/10.1103/PhysRevB.98.085127.

[54] D. Vanderbilt, Soft self-consistent pseudopotentials in a generalized eigenvalue formalism, Phys. Rev. B 41 (1990) 7892–7895, http://dx.doi.org/10.1103/PhysRevB.41.7892.

[55] Ultrasoft pseudopotentials for the H, C, O, Mn, and Ni atoms were taken from the Quantum ESPRESSO Pseudopotential Download Page at http://www.quantum-espresso.org/pseudopotentials (files: `H.pbe-rrkjus.UPF`, `C.pbe-rrkjus.UPF`, `O.pbe-rrkjus.UPF`, `Mn.pbe-sp-van.UPF`, and `Ni.pbe-nd-rrkjus.UPF`), 2021.

[56] H.J. Monkhorst, J.D. Pack, Special points for Brillouin-zone integrations, Phys. Rev. B 13 (12) (1976) 5188–5192, http://dx.doi.org/10.1103/PhysRevB.13.5188.

[57] M. Methfessel, A.T. Paxton, High-precision sampling for Brillouin-zone integration in metals, Phys. Rev. B 40 (6) (1989) 3616–3621, http://dx.doi.org/10.1103/PhysRevB.40.3616.

[58] N. Marzari, D. Vanderbilt, A. De Vita, M.C. Payne, Thermal contraction and disordering of the Al(110) surface, Phys. Rev. Lett. 82 (16) (1999) 3296–3299, http://dx.doi.org/10.1103/PhysRevLett.82.3296.

[59] S. Baroni, S. de Gironcoli, A. Dal Corso, P. Giannozzi, Phonons and related crystal properties from density-functional perturbation theory, Rev. Modern Phys. 73 (2001) 515–562, http://dx.doi.org/10.1103/RevModPhys.73.515.

[60] G. Henkelman, H. Jónsson, Improved tangent estimate in the nudged elastic band method for finding minimum energy paths and saddle points, J. Chem. Phys. 113 (22) (2000) 9978–9985, http://dx.doi.org/10.1063/1.1323224.

[61] G. Henkelman, B.P. Uberuaga, H. Jónsson, A climbing image nudged elastic band method for finding saddle points and minimum energy paths, J. Chem. Phys. 113 (22) (2000) 9901–9904, http://dx.doi.org/10.1063/1.1329672.

[62] J.C. Campuzano, R.G. Greenler, The adsorption sites of CO on Ni(111) as determined by infrared reflection-absorption spectroscopy, Surf. Sci. 83 (1) (1979) 301–312, http://dx.doi.org/10.1016/0039-6028(79)90495-3.

[63] A. Politano, G. Chiarello, Vibrational investigation of catalyst surfaces: Change of the adsorption site of CO molecules upon coadsorption, J. Phys. Chem. C 115 (28) (2011) 13541–13553, http://dx.doi.org/10.1021/jp202212a.

[64] B. Voigtländer, D. Bruchmann, S. Lehwald, H. Ibach, Structure and adsorbate-adsorbate interactions of the compressed Ni(110)-(2×1)CO structure, Surf. Sci. 225 (1) (1990) 151–161, http://dx.doi.org/10.1016/0039-6028(90)90433-9.

[65] G. Zhou, H. Liu, K. Cui, A. Jia, G. Hu, Z. Jiao, Y. Liu, X. Zhang, Role of surface Ni and Ce species of Ni/CeO_2 catalyst in CO_2 methanation, Appl. Surf. Sci. 383 (2016) 248–252, http://dx.doi.org/10.1016/j.apsusc.2016.04.180.

[66] P.J. Feibelman, B. Hammer, J.K. Nørskov, F. Wagner, M. Scheffler, R. Stumpf, R. Watwe, J. Dumesic, The CO/Pt(111) puzzle, J. Phys. Chem. B 105 (18) (2001) 4018–4025, http://dx.doi.org/10.1021/jp002302t.

[67] P. Janthon, F. Viñes, J. Sirijaraensre, J. Limtrakul, F. Illas, Adding pieces to the CO/Pt(111) puzzle: The role of dispersion, J. Phys. Chem. C 121 (7) (2017) 3970–3977, http://dx.doi.org/10.1021/acs.jpcc.7b00365.

[68] V. Sumaria, L. Nguyen, F.F. Tao, P. Sautet, Optimal packing of CO at a high coverage on Pt(100) and Pt(111) surfaces, ACS Catal. 10 (16) (2020) 9533–9544, http://dx.doi.org/10.1021/acscatal.0c01971.

[69] A.J. Bradley, J. Thewlis, W.L. Bragg, The crystal structure of α-manganese, P. R. Soc. Lond. A-Conta. 115 (771) (1927) 456–471, http://dx.doi.org/10.1098/rspa.1927.0103.

[70] M. Dlouhy, A. Kokalj, How adsorbed H, O, OH, and Cl affect plain adsorption of imidazole on copper, Corros. Sci. 205 (2022) 110443, http://dx.doi.org/10.1016/j.corsci.2022.110443.

[71] S. Grimme, J. Antony, S. Ehrlich, H. Krieg, A consistent and accurate ab initio parametrization of density functional dispersion correction (DFT-D) for the 94 elements H-Pu, J. Chem. Phys. 132 (15) (2010) 154104, http://dx.doi.org/10.1063/1.3382344.

[72] A. Michaelides, Z.-P. Liu, C.J. Zhang, A. Alavi, D.A. King, P. Hu, Identification of general linear relationships between activation energies and enthalpy changes for dissociation reactions at surfaces, J. Am. Chem. Soc. 125 (13) (2003) 3704–3705, http://dx.doi.org/10.1021/ja027366r.